AIAA JOURNAL
Vol. 45, No. 12, December 2007

Installation Effects on the Flow and Noise of Wing Mounted Jets

Nikolai N. Pastouchenko* and Christopher K. W. Tam†
Florida State University, Tallahassee, Florida 32306-4510

DOI: 10.2514/1.26647

It is known experimentally that a jet mounted under a wing generates more noise than the same jet in isolation. The excess noise is referred to as installation noise. Installation noise is largely of aerodynamic origin. The principal mechanism is believed to be the impact of the downwash of the wing flap on the jet flow. The downwash causes the jet to deflect downward and to distort laterally. This brings about an increase in turbulence in the jet. The increase in the level of turbulence, in turn, leads to the emission of additional noise. The modeling and computation of the downwash, the distorted jet flow, and the excess noise radiation are the objectives of this investigation. It will be shown that calculated results at high frequencies compare well with experimental measurements.

I. Introduction

IT IS known experimentally, since the late 1970s, that a jet installed under a wing of an aircraft radiates more noise than the same jet in a standalone condition. The excess noise is the propulsion-airframe integration noise or commonly referred to as installation noise. When a jet is placed near a wing, there is an increase in noise in the flyover directions because of the reflection of sound by the wing. Here, installation noise includes not merely the noise increase due to the reflection of sound by the wing. The major part of this noise is generated aerodynamicly by the nonlinear interaction between the flow around the wing flap and the jet. In this work, our primary interest is to model and to predict installation noise of aerodynamic origin. Installation noise increases not only the total aircraft noise in the flyover plane but also in the sideline directions. It is especially important during landings and takeoffs when the flaps are down.

During the 1980s, a number of experiments were carried out trying to quantify the characteristics and intensity of installation noise [1–4]. Most of these experiments involved the measurements of the jet alone noise and the noise when the jet was placed near a model of an aircraft wing inside an anechoic chamber. The experimental measurements by Wang [2] were the most systematic. In his experiment, a scaled model of the wing of a DC-10 aircraft was used. Large noise increase was observed in the flyover plane in the low-frequency part of the spectrum. The increase in high-frequency noise was less. In directions at small exhaust angles, the installation noise intensity was quite low. In the sideline, the radiated noise characteristics, on the other hand, were quite different. Overall, the measured data indicated that installation noise had a unique spectral shape and a directional pattern of its own.

Recently, there is a renewed interest in propulsion-airframe integration noise. Mead and Strange [5] investigated the under-the-wing installation effects on jet noise with special emphasis on the sideline directions. Their interest in the sideline was motivated by the experience that it was generally more difficult to meet legislative limit on sideline noise level requirements. They reported the measurement of high installation noise level in the low-frequency range.

One drawback of the Mead and Strange experiment [5], as well as most of the previous works, is that the experiments were carried out in static conditions. Upon realizing that the effect of forward flight is extremely important in the interaction between the flow around the wing flap and the jet, a series of new experiments on installation noise was conducted by engineers of The Boeing Company (Shivashankara and Blackner [6], Blackner and Bhat [7], and Bhat and Blackner [8]). They employed an open wind tunnel at $M = 0.28$ to simulate the forward motion of the aircraft. By using elliptic mirror microphones and the newly developed phase-array microphones, they were able to obtain noise source location maps as well as far-field noise data.

In the Boeing study, summarized by Bhat [9], the variation and sensitivity of installation noise to a range of flow parameters, wing-flap settings, jet engine location, and pitching angle were investigated. Installation noise up to 6 dB across a wide band of frequency was measured. This is a very large increase in noise. It can easily negate the gains of recent successes in suppressing other components of airframe noise.

Next is a summary of the important findings of the Boeing investigation.

1) The presence of the airframe increases jet noise significantly.

2) The noise increase follows monotonically with increasing flap deflection. Flap deflection has the largest effect on installation noise.

3) Noise levels are insensitive to engine installation location within Boeing's current envelope of possibilities at takeoff flap setting.

4) A wide bifurcation can contribute to a slight increase in noise level.

5) Pitching the nozzle up toward the wing can increase the noise levels, whereas pitching the nozzle away from the wing has little benefit.

In conjunction with their experimental study, an empirical installation noise prediction method was developed by Bhat and Blackner [8]. The approach of Bhat and Blackner followed an earlier work at Boeing by Lu [10] for the prediction of noise from isolated coaxial jets in ambient flow. The methodology is entirely empirical. Only a limited amount of flow physics was incorporated into the formulation of the prediction code. The predicted noise spectra were in fair agreement with measurements at low to moderate frequencies. However, there were significant discrepancies in the higher frequency range of all the measured spectra.

Most recently, there have been extensive experimental and developmental works on jet installation noise [11–14]. The focus of these series of works, however, is not so much in obtaining a better understanding of the mechanisms responsible for installation noise, but in finding a method to reduce installation noise

Presented as Paper 604 at the 43rd AIAA Aerospace Science Meeting, Reno, Nevada, 10–13 January 2005; received 19 July 2006; revision received 29 November 2006; accepted for publication 17 November 2006.

*Postdoctoral Research Associate, Department of Mathematics.

†Robert O. Lawton Distinguished Professor, Department of Mathematics, Fellow AIAA.

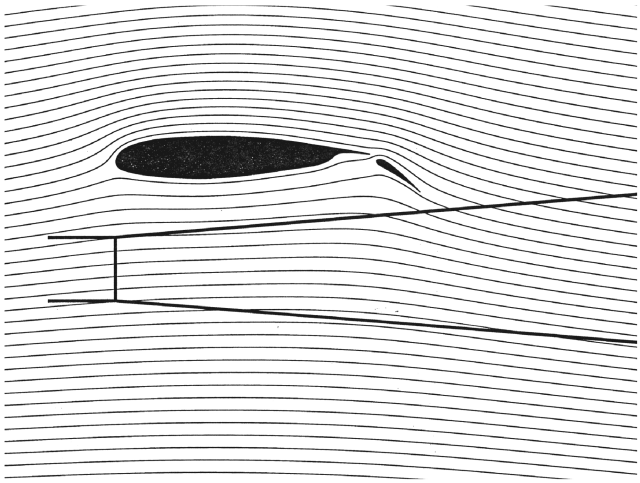

Fig. 1 Streamlines showing the impact of downwash on an under-the-wing mounted jet.

empirically. These are laudable efforts but are beyond the scope of this work.

The primary objective of this investigation is to develop a computational model to calculate installation effects on the flow and noise of an under-the-wing mounted dual-stream jet. Installation of a jet engine under a wing in forward flight leads to very complex fluid dynamic interaction between the flow around the wing flap and the jet. To compute the entire interaction is beyond the scope of this work. Based on the Boeing results, we focus our attention mainly on the impact of the downwash of the wing flap on the jet plume. Figure 1 shows the streamlines around an airfoil at zero angle of attack and a flap at a deflection angle of 35 deg. The forward flight Mach number is 0.2. Superimposed on this figure are the outlines of a nozzle and that of a Mach 0.8 jet at a temperature ratio of 1.54. This figure indicates that the downwash, which is especially strong when the flap is fully deployed, could cause the jet to deflect downward and distort laterally. In the present investigation, a simple mathematical model is adopted in the computation. Only the effect of downwash on the jet is considered. The effect of the presence of the jet on the wing-flap flow will be neglected. The large deflection and distortion of the jet caused by the strong downwash lead to an increase in the level of turbulence in the jet. This, in turn, leads to an increase in jet noise radiation. It is known that there are two principal components of jet mixing noise. One component is generated by the large turbulence structures of the jet flow and the other component is generated by the fine-scale turbulence. In this work, only the installation noise from the enhanced fine-scale turbulence is calculated. Comparisons with experimental measurements will be reported.

The rest of the paper is as follows. First, the downwash from the wing flap is calculated by solving the Euler equations. The distorted jet mean flow is then calculated by a parabolized RANS $k-\varepsilon$ turbulence model taking into consideration the downwash as a side boundary condition. The computed mean flow and the turbulence information from the $k-\varepsilon$ model are subsequently used to calculate the radiated noise through the extended Tam and Auriault fine-scale turbulence noise theory [15,16] Finally, the installation noise is determined by subtracting from the calculated noise the noise of the same jet in isolation.

II. Downwash from a Wing Flap in High-Lift Configuration

For the purpose of calculating the downwash of a wing-flap combination in an approach configuration, an inviscid flow model is used. The wing will be taken as two-dimensional. The governing equations are the Euler and energy equations:

$$\frac{\partial \rho}{\partial t}+\rho\left(\frac{\partial u}{\partial x}+\frac{\partial v}{\partial y}\right)+u\frac{\partial \rho}{\partial x}+v\frac{\partial \rho}{\partial y}=0 \tag{1}$$

$$\frac{\partial u}{\partial t}+u\frac{\partial u}{\partial x}+v\frac{\partial u}{\partial y}+\frac{1}{\rho}\frac{\partial p}{\partial x}=0 \tag{2}$$

$$\frac{\partial v}{\partial t}+u\frac{\partial v}{\partial x}+v\frac{\partial v}{\partial y}+\frac{1}{\rho}\frac{\partial p}{\partial y}=0 \tag{3}$$

$$\frac{\partial p}{\partial t}+u\frac{\partial p}{\partial x}+v\frac{\partial p}{\partial y}+\gamma p\left(\frac{\partial u}{\partial x}+\frac{\partial v}{\partial y}\right)=0 \tag{4}$$

The boundary condition on the surface of the wing flap is

$$un_x+vn_y=0 \tag{5}$$

where $\boldsymbol{n}=(n_x,n_y)$ is the unit normal of the wing-flap surface.

In the present study, Eqs. (1–4) are solved by the multi-size-mesh multi-time-step dispersion-relation-preserving scheme [17] on a Cartesian grid as shown in Fig. 2. The finest mesh is employed in the block containing the airfoil and the flap. This very fine mesh is used to resolve the geometrical details of the two solid bodies. Away from the airfoil, the flow becomes more and more smooth. Thus, there is a gradual relaxation of the resolution requirement. Accordingly, the mesh size and the corresponding time step used in the computation increase by a factor of two each time one moves to the next outer block. In this way, the flow over a fairly large domain can be computed with a reasonable amount of computing time.

To enforce the boundary condition (5), the Cartesian boundary treatment method proposed by Kurbatskii and Tam [18] is used. At the inflow and lower boundaries of the computation domain, the radiation boundary condition of Tam and Webb [19] is enforced. At the right and top boundaries, the Tam and Webb [19] outflow boundary conditions are implemented. The computation starts with a uniform flow and time marched to steady state. To promote fast convergence, the method of accelerated convergence to steady state proposed by Tam and Dong [20] is applied. The idea of the method is to perform a "canceling-the-residue" operation. In a numerical computation, the best one can do is to make the difference between the numerical and the exact solution to be on the order of a tenth of a percent. In other words, further time marching computation could be a waste of effort in terms of improving the accuracy of the solution, once the residual reaches a level on the order of 10^{-5}. With this in mind, it is possible to add a term that is exactly equal in magnitude but opposite in sign to the residual, at this stage, to the right side of each of the governing equations. These are terms of order 10^{-5} or less and

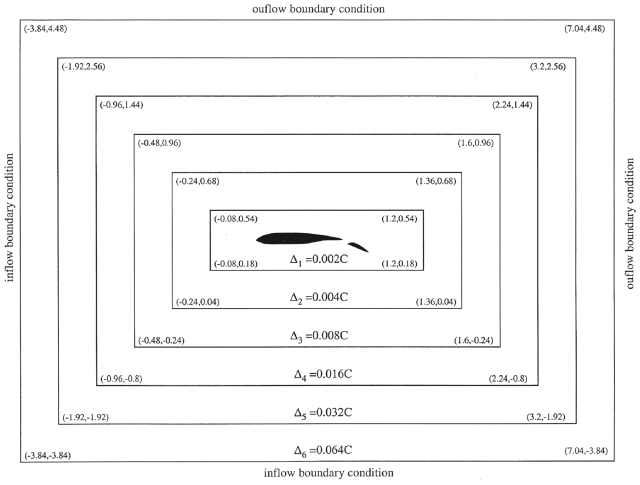

Fig. 2 Computation domain for calculating the downwash of an airfoil and flap.

would, therefore, not materially affect the accuracy of the steady-state numerical solution. The added terms may be regarded as minute artificial distributed sources of fluid, momentum, or heat. The consequence of adding these source terms is to cancel the residuals instantly to zero. Of course, for the multilevel matching scheme, the residuals of the scheme are greatly reduced in this way but they would not be exactly equal to zero at the next time level. Numerical experiments indicate that when the preceding canceling-the-residual procedure is performed, the overall residuals of the computation drop almost instantaneously by several orders of magnitude. This operation may be applied repeatedly until the residuals are driven to machine round-off error.

III. Computation of the Mean Flow of an Under-the-Wing Mounted Jet

We will use the Reynolds-averaged Navier–Stokes equations (RANS) together with the $k-\varepsilon$ turbulence model to calculate the mean flow of an under-the-wing mounted dual-stream jet. It has been pointed out that the standard $k-\varepsilon$ model has a number of deficiencies. To remedy the shortcomings of the model, we will include the Pope correction [21] for three-dimensional flows, the Sarkar and Lakshmanan correction [22] for convective Mach number effects, and the Tam and Ganesan [23] correction for density gradients existing in hot jets.

A. Parabolized RANS Equations

For convenience, nondimensional variables with respect to the following scales are used.

length scale $= D_p$ (diameter of primary nozzle)
velocity scale $= u_p$ (fully expanded velocity of primary jet)
time scale $= D_p/u_p$
density scale $= \rho_p$ (density of primary nozzle)
pressure scale $= \rho_p u_p^2$
temperature scale $= T_p$ (fully expanded temperature of primary jet)
scale for k and $\tau_{ij} = u_p^2$
scale for $\varepsilon = u_p^3/D_p$
scale for $\nu_t = D_p u_p$

The steady-state RANS equations, including the modified $k-\varepsilon$ turbulence model in Cartesian tensor notation, are

$$\frac{\partial u_j}{\partial x_j} - \frac{u_j}{T}\frac{\partial T}{\partial x_j} + \frac{u_j}{p}\frac{\partial p}{\partial x_j} = 0 \tag{6}$$

$$\rho u_j \frac{\partial u_i}{\partial x_j} = -\frac{\partial p}{\partial x_i} - \frac{\partial}{\partial x_j}(\rho\tau_{ij}) \tag{7}$$

$$\rho u_j \frac{\partial T}{\partial x_j} = -\gamma(\gamma-1)M_p^2 p\frac{\partial u_j}{\partial x_j} + \gamma(\gamma-1)M_p^2\rho\varepsilon + \frac{1}{\sigma_T}\frac{\partial}{\partial x_j}\left(\rho\nu_t\frac{\partial T}{\partial x_j}\right) \tag{8}$$

$$\rho u_j \frac{\partial k}{\partial x_j} = -\rho\tau_{ij}\frac{\partial u_i}{\partial x_j} - \rho\varepsilon + \frac{1}{\sigma_k}\frac{\partial}{\partial x_j}\left(\rho\nu_t\frac{\partial k}{\partial x_j}\right) \tag{9}$$

$$\rho u_j \frac{\partial \varepsilon_s}{\partial x_j} = -c_{\varepsilon 1}\frac{\varepsilon_s}{k}\rho\tau_{ij}^{(s)}\frac{\partial u_i}{\partial x_j} - (c_{\varepsilon 2} - c_{\varepsilon 3}\chi)\rho\frac{\varepsilon_s^2}{k} + \frac{1}{\sigma_\varepsilon}\frac{\partial}{\partial x_j}\left(\rho\nu_t^{(s)}\frac{\partial \varepsilon_s}{\partial x_j}\right) \tag{10}$$

$$p = \frac{\rho T}{\gamma M_p^2} \tag{11}$$

$$\varepsilon = \varepsilon_s\left(1 + \alpha_1 M_t^2\right), \qquad M_t^2 = \frac{2kM_p^2}{T} \tag{12}$$

$$\tau_{ij} = \frac{2}{3}k\delta_{ij} - \nu_t\left(\frac{\partial u_i}{\partial x_j} + \frac{\partial u_j}{\partial x_i} - \frac{2}{3}\frac{\partial u_k}{\partial x_k}\delta_{ij}\right) \tag{13a}$$

$$\tau_{ij}^{(s)} = \frac{2}{3}k\delta_{ij} - \nu_t^{(s)}\left(\frac{\partial u_i}{\partial x_j} + \frac{\partial u_j}{\partial x_i} - \frac{2}{3}\frac{\partial u_k}{\partial x_k}\delta_{ij}\right) \tag{13b}$$

$$\nu_t = c_\mu\frac{k^2}{\varepsilon} + \nu_\rho, \qquad \nu_t^{(s)} = c_\mu\frac{k^2}{\varepsilon_s} + \nu_\rho^{(s)} \tag{14a}$$

$$\nu_\rho = \begin{cases} c_\rho\frac{k^{7/2}}{\varepsilon^2}\frac{|\nabla\rho\cdot\nabla u|}{\rho|\nabla u|}, & \text{if } (\nabla\rho)\cdot(\nabla u)\text{is negative} \\ 0 & \text{otherwise} \end{cases} \tag{14b}$$

$$\nu_\rho^{(s)} = \begin{cases} c_\rho\frac{k^{7/2}}{\varepsilon_s^2}\frac{|\nabla\rho\cdot\nabla u|}{\rho|\nabla u|}, & \text{if } (\nabla\rho)\cdot(\nabla u) \text{ is negative} \\ 0, & \text{otherwise} \end{cases} \tag{14c}$$

$$\chi = \omega_{ij}\omega_{jk}s_{ki} \tag{15a}$$

$$\omega_{ij} = \frac{1}{2}\frac{k}{\varepsilon_s}\left(\frac{\partial u_i}{\partial x_j} - \frac{\partial u_j}{\partial x_i}\right) \tag{15b}$$

$$s_{ij} = \frac{1}{2}\frac{k}{\varepsilon_s}\left(\frac{\partial u_i}{\partial x_j} + \frac{\partial u_j}{\partial x_i}\right) \tag{15c}$$

The empirical constants of the preceding equations are assigned values as follows:

$$c_\mu = 0.0874, \qquad c_{\varepsilon 1} = 1.40, \qquad c_{\varepsilon 2} = 2.02, \qquad c_{\varepsilon 3} = 0.822$$
$$\gamma\sigma_T = Pr(\text{turbulent Prandtl number}) = 0.422 \qquad \sigma_k = 0.324$$
$$\sigma_\varepsilon = 0.377, \qquad \alpha_1 = 0.518, \qquad c_\rho = 0.035$$

It is advantageous to separate the solution into two parts as

$$\begin{bmatrix} p \\ T \\ u_i \end{bmatrix} = \begin{bmatrix} p^{(a)} \\ T^{(a)} \\ u_i^{(a)} \end{bmatrix} + \begin{bmatrix} \hat{p} \\ \hat{T} \\ \hat{u}_i \end{bmatrix} \tag{16}$$

where the quantities with superscript (a) are the downwash flow solution found in the preceding section. Here, it will be assumed that this solution has been completed at this stage and that the main effort now is to calculate $(\hat{p}, \hat{T}, \hat{u}_i)$. The principal reason for separating the solution in the form of Eq. (16) is to allow a clear and simple prescription of boundary conditions. Here, the natural boundary conditions are

$$(\hat{p}, \hat{T}, \hat{u}_i, k, \varepsilon) \to 0, \qquad \text{away from the jet} \tag{17}$$

In this investigation, the aim is to develop a set of parabolized equations for the determination of unknown variables $(\hat{p}, \hat{T}, \hat{u}_i, k, \varepsilon)$. The approach is similar to previous works [16,24,25]. But because of the downwash flow, the resulting equations are different. To simplify the derivation of the parabolized equations, it will be assumed that the downwash flow is practically incompressible, i.e.,

$$\frac{\partial u_j^{(a)}}{\partial x_j} \cong 0 \tag{18}$$

and that ρ in Eqs. (2) and (3) may be substituted with ρ_∞. This approximation is justified because the forward flight Mach number is low subsonic.

In [16,24,25], the fluid density is eliminated by using the equation of state in favor of pressure p and temperature T. Here, the same strategy is followed. Thus, Eq. (16), which is the continuity equation, is used to compute $\hat{p}$. Substitution of Eq. (16) into Eq. (6), and after some algebraic manipulation, it is straightforward to derive a parabolized equation for $\hat{p}$ in Cartesian coordinates. The x axis is in the flow direction

$$\frac{\partial \hat{p}}{\partial x} = -\frac{\partial p^{(a)}}{\partial x} + \frac{1}{(\hat{u}+u^{(a)})}\left[-(\hat{v}+v^{(a)})\left(\frac{\partial \hat{p}}{\partial y}+\frac{\partial p^{(a)}}{\partial y}\right) - \hat{w}\frac{\partial \hat{p}}{\partial z} - (\hat{p}+p^{(a)})\left(\frac{\partial \hat{u}}{\partial x}+\frac{\partial \hat{v}}{\partial y}+\frac{\partial \hat{w}}{\partial z}\right) + \frac{\rho}{\gamma M_p^2}\left((\hat{u}+u^{(a)})\frac{\partial \hat{T}}{\partial x}+(\hat{v}+v^{(a)})\frac{\partial \hat{T}}{\partial y}+\hat{w}\frac{\partial \hat{T}}{\partial z}\right)\right] \tag{19}$$

where $(\hat{u},\hat{v},\hat{w})$ are the Cartesian velocity components. It is to be noted that the terms $\partial\hat{u}/\partial x$ and $\partial\hat{T}/\partial x$ on the right side of Eq. (19) are given by the x momentum and the energy equation [see Eqs. (20) and (23)], so that the right side does not have any unknown x derivative.

On following the steps in the derivation of Eq. (19) and by making use of the approximation in Eq. (18) and boundary layer argument, i.e., $\partial/\partial y,\ \partial/\partial z \gg \partial/\partial x$, a full set of parabolized equations for variables $(\hat{u},\hat{v},\hat{w},\hat{T},k,\varepsilon)$ can be derived readily. These equations when written out are as follows:

$$\frac{\partial \hat{u}}{\partial x} = \frac{1}{(\hat{u}+u^{(a)})}\left\{-(\hat{v}+v^{(a)})\frac{\partial \hat{u}}{\partial y} - \hat{w}\frac{\partial \hat{u}}{\partial z} - \hat{u}\frac{\partial u^{(a)}}{\partial x} - \hat{v}\frac{\partial u^{(a)}}{\partial y} + \frac{\rho-\rho_\infty}{\rho\rho_\infty}\frac{\partial p^{(a)}}{\partial x} - \frac{1}{\rho}\left[\frac{\partial(\rho\hat{\tau}_{xy})}{\partial y}+\frac{\partial(\rho\hat{\tau}_{xz})}{\partial z}\right]\right\} \tag{20}$$

$$\frac{\partial \hat{v}}{\partial x} = \frac{1}{(\hat{u}+u^{(a)})}\left\{-(\hat{v}+v^{(a)})\frac{\partial \hat{v}}{\partial y} - \hat{w}\frac{\partial \hat{v}}{\partial z} - \hat{u}\frac{\partial v^{(a)}}{\partial x} - \hat{v}\frac{\partial v^{(a)}}{\partial y} - \frac{1}{\rho}\frac{\partial \hat{p}}{\partial y} + \frac{\rho-\rho_\infty}{\rho\rho_\infty}\frac{\partial p^{(a)}}{\partial y} - \frac{1}{\rho}\left[\frac{\partial(\rho\hat{\tau}_{yy})}{\partial y}+\frac{\partial(\rho\hat{\tau}_{yz})}{\partial z}\right]\right\} \tag{21}$$

$$\frac{\partial \hat{w}}{\partial x} = \frac{1}{(\hat{u}+u^{(a)})}\left\{-(\hat{v}+v^{(a)})\frac{\partial \hat{w}}{\partial y} - \hat{w}\frac{\partial \hat{w}}{\partial z} - \frac{1}{\rho}\frac{\partial \hat{p}}{\partial z} - \frac{1}{\rho}\left[\frac{\partial(\rho\hat{\tau}_{zy})}{\partial y}+\frac{\partial(\rho\hat{\tau}_{zz})}{\partial z}\right]\right\} \tag{22}$$

$$\frac{\partial \hat{T}}{\partial x} = \frac{1}{(\hat{u}+u^{(a)})}\left\{-(\hat{v}+v^{(a)})\frac{\partial \hat{T}}{\partial y} - \hat{w}\frac{\partial \hat{T}}{\partial z} - (\gamma-1)(\hat{T}+T_\infty)\left(\frac{\partial \hat{u}}{\partial x}+\frac{\partial \hat{v}}{\partial y}+\frac{\partial \hat{w}}{\partial z}\right) + \gamma(\gamma-1)M_p^2\varepsilon + \frac{\gamma}{P_r\rho}\left[\frac{\partial}{\partial y}\left(\rho\nu_t\frac{\partial \hat{T}}{\partial y}\right)+\frac{\partial}{\partial z}\left(\rho\nu_t\frac{\partial \hat{T}}{\partial z}\right)\right]\right\} \tag{23}$$

$$\frac{\partial k}{\partial x} = \frac{1}{(\hat{u}+u^{(a)})}\left\{-(\hat{v}+v^{(a)})\frac{\partial k}{\partial y} - \hat{w}\frac{\partial k}{\partial z} - \tau_{xy}\left(\frac{\partial \hat{u}}{\partial y}+\frac{\partial u^{(a)}}{\partial y}\right) - \tau_{xz}\frac{\partial \hat{u}}{\partial z} - \tau_{yy}\left(\frac{\partial \hat{v}}{\partial y}+\frac{\partial v^{(a)}}{\partial y}\right) - \tau_{yz}\frac{\partial \hat{v}}{\partial z} - \tau_{zy}\frac{\partial \hat{w}}{\partial y} - \tau_{zz}\frac{\partial \hat{w}}{\partial z} - \varepsilon + \frac{1}{\rho\sigma_k}\left[\frac{\partial}{\partial y}\left(\rho\nu_t\frac{\partial k}{\partial y}\right)+\frac{\partial}{\partial z}\left(\rho\nu_t\frac{\partial k}{\partial z}\right)\right]\right\} \tag{24}$$

$$\frac{\partial \varepsilon_s}{\partial x} = \frac{1}{(\hat{u}+u^{(a)})}\left\{-(\hat{v}+v^{(a)})\frac{\partial \varepsilon_s}{\partial y} - \hat{w}\frac{\partial \varepsilon_s}{\partial z} - c_{\varepsilon 1}\frac{\varepsilon_s}{k}\left[\tau_{xy}^{(s)}\left(\frac{\partial \hat{u}}{\partial y}+\frac{\partial u^{(a)}}{\partial y}\right)+\tau_{xz}^{(s)}\frac{\partial \hat{u}}{\partial z}+\tau_{yy}^{(s)}\left(\frac{\partial \hat{v}}{\partial y}+\frac{\partial v^{(a)}}{\partial y}\right) + \tau_{yz}^{(s)}\frac{\partial \hat{v}}{\partial z}+\tau_{zy}^{(s)}\frac{\partial \hat{w}}{\partial y}+\tau_{zz}^{(s)}\frac{\partial \hat{w}}{\partial z}\right] - (c_{\varepsilon 2}-c_{\varepsilon 3}\chi)\frac{\varepsilon_s^2}{k} + \frac{1}{\rho\sigma_\varepsilon}\left[\frac{\partial}{\partial y}\left(\rho\nu_t^{(s)}\frac{\partial \varepsilon_s}{\partial y}\right)+\frac{\partial}{\partial z}\left(\rho\nu_t^{(s)}\frac{\partial \varepsilon_s}{\partial z}\right)\right]\right\} \tag{25}$$

where ρ_∞ and T_∞ are the density and temperature of the freestream. To complete the parabolized system, all the x derivatives in the stress terms and χ of Eqs. (13) and (15) are dropped. They are small compared with the y and z derivative terms.

B. Radiation or Outgoing Wave Boundary Conditions

To compute the solution of the parabolized system of Eqs. (19–25), the four-level dispersion-relation-preserving (DRP) scheme [19] is used to march the solution downstream in the x direction. Here, the x axis is treated as the time axis in the DRP methodology. The solution is contained in planes parallel to the $x-z$ plane. The computation domain in these parallel planes is finite and does not extend too far from the jet flow. For this reason, boundary condition (17) for the variables $(\hat{p},\hat{T},\hat{u}_i)$ cannot be implemented. As in previous work involving the computation of jet mean flow through parabolized equations [26], a set of radiation/outgoing wave boundary conditions is used at the edge of the computation domain. This set of boundary conditions is derived by first finding an asymptotic solution (an approximate one if necessary) of the parabolized equations in the limit $(y^2+z^2)^{1/2}$ is large. The radiation boundary conditions are then found by eliminating the unknown function of the asymptotic solution through cross differentiation. In this work, this procedure has been carried out with the aid of a frozen coefficient approximation. The boundary conditions for large $(y^2+z^2)^{1/2}$ actually implemented in this work are

$$u^{(a)}\frac{\partial \hat{u}}{\partial x} + v^{(a)}\frac{\partial \hat{u}}{\partial y} = 0 \tag{26}$$

$$u^{(a)}\frac{\partial \hat{v}}{\partial x} + v^{(a)}\frac{\partial \hat{v}}{\partial y} + a_\infty\left[\frac{z}{(z^2+y^2)^{\frac{1}{2}}}\frac{\partial \hat{v}}{\partial z}+\frac{y}{(z^2+y^2)^{\frac{1}{2}}}\frac{\partial \hat{v}}{\partial y} + \frac{z^2}{(y^2+z^2)^{\frac{3}{2}}}\left(\hat{v}-\frac{v^{(a)}}{u^{(a)}}\hat{u}\right) - \frac{yz}{(y^2+z^2)^{\frac{3}{2}}}\hat{w}\right] + \frac{\hat{v}-v^{(a)}\hat{u}/u^{(a)}}{(y^2+z^2)^{\frac{1}{2}}} = 0 \tag{27}$$

$$u^{(a)}\frac{\partial \hat{w}}{\partial x} + v^{(a)}\frac{\partial \hat{w}}{\partial y} + a_\infty\left[\frac{z}{(y^2+z^2)^{\frac{1}{2}}}\frac{\partial \hat{w}}{\partial z}+\frac{y}{(y^2+z^2)^{\frac{1}{2}}}\frac{\partial \hat{w}}{\partial y} + \frac{y^2}{(y^2+z^2)^{\frac{3}{2}}}\hat{w} - \frac{yz}{(y^2+z^2)^{\frac{3}{2}}}\left(\hat{v}-\frac{v^{(a)}}{u^{(a)}}\hat{u}\right)\right] + \frac{\hat{w}}{(y^2+z^2)^{\frac{1}{2}}} = 0 \tag{28}$$

$$\left[u^{(a)}\frac{\partial}{\partial x} + v^{(a)}\frac{\partial}{\partial y} + a_\infty\left(\frac{z}{(y^2+z^2)^{\frac{1}{2}}}\frac{\partial}{\partial z}+\frac{y}{(y^2+z^2)^{\frac{1}{2}}}\frac{\partial}{\partial y}\right) + \frac{1}{(y^2+z^2)^{\frac{1}{2}}}\right]\begin{bmatrix}\hat{p}\\ \hat{T}\end{bmatrix} = 0 \tag{29}$$

$$k = \varepsilon_s = 0 \tag{30}$$

C. Numerical Results

Consider an under-the-wing mounted dual-stream jet in a configuration as shown in Fig. 3. The nozzle has an area ratio of three

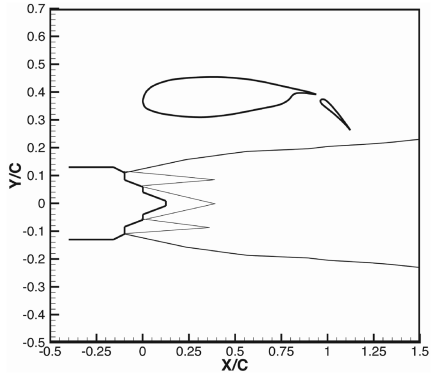

Fig. 3 Installed jet model; C = length of wing chord.

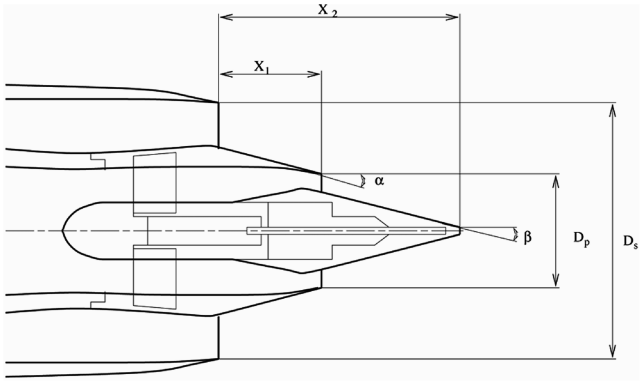

Fig. 4 Dual-stream nozzle with an external plug of the Boeing experiments; area ratio = 3, $D_s/D_p = 1.9$, $X_1/D_p = 0.85$, $X_2/D_p = 1.8$, $\alpha = 14$ deg, $\beta = 15$ deg.

and is designed to operate at a bypass ratio of six with primary jet Mach number $M_p = 0.762$, temperature ratio $T_p/T_a = 2.9$ (T_p is the reservoir temperature of the primary jet, T_a is the ambient temperature), and secondary jet Mach number $M_s = 0.9$, and temperature ratio $T_p/T_a = 1.2$. The geometry of the nozzle that is used in the Boeing experiments [8] is shown in Fig. 4. To illustrate the effect of wing-flap downwash on the jet flow, we consider the case of forward flight Mach number 0.28. As shown in Fig. 3, the nozzle exit is located directly under the leading edge of the wing, so that there is little downwash flow. The trailing edge of the deflected flap is located at a distance of approximately $3D_s$ (D_s= diameter of secondary nozzle) downstream. At this location, the downwash is at the maximum intensity. For the jet mean flow calculation, use is made of the oblique Cartesian coordinates method of [22]. Computation starts at the exit of the secondary nozzle and marches downstream to the tip of the plug nozzle. This solution provides the starting values for the present computation using parabolized RANS Eqs. (19–25) and boundary conditions (26–31).

Figure 5 shows the computed contours of constant axial velocity at different distances downstream on planes parallel to the nozzle exit plane or the $y - z$ plane. The two black concentric circles in Figs. 5a and 5f are the inner and outer boundaries of the primary jet at the nozzle exit. They provide a reference to show the downward displacement of the jet flow. Figures 5a and 5b show the axial velocity contours at $x/D_s = 1.5$ and 3.5. The contours are nearly circular, indicating the fact that the impact of wing-flap downwash has not been felt by the jet flow. Figures 5c–5f show a gradual downward displacement of the jet. At the same time, the jet is distorted laterally. The downward deflection and lateral distortion are responsible for an increase in turbulence level in the jet. Figure 6 shows the computed axial velocity profiles of the jet in the vertical symmetry plane through the center of the jet at various distances downstream. These profiles are shown in dotted lines. For comparison purposes, the profiles of the same jet in a standalone condition are shown in full lines. It is readily seen that the velocity profiles are displaced gradually downward. In addition, the profiles are no longer symmetric with respect to the maximum velocity point. In a Boeing experiment [7], the downward displacement, as well as the lateral distortion, of the jet were observed. However, not enough quantitative information was provided to allow a direct comparison with computed results.

IV. Computation of Installation Noise and Comparison with Experiment

Once the mean flow of an installed jet and the values of k and ε are computed, the fine-scale turbulence noise from the jet may be calculated by the extended Tam and Auriault theory [15,16]. The far-field noise spectrum $S(R, \Theta, \phi, fD_p/u_p)$ at a point with spherical polar coordinates (R, Θ, ϕ), with respect to a polar coordinate system centered at the nozzle exit with the polar axis coinciding with the x axis, is given by (in decibels)

$$S\left(R, \Theta, \phi, \frac{fD_p}{u_p}\right) = 10\log\left[\frac{4\pi S(\mathbf{x}, \omega)}{p_{\text{ref}}^2 (D_p/u_p)}\right] \tag{31}$$

where

$$S(\mathbf{x}, \omega) = \frac{4\pi^3}{(\ell_n 2)^{3/2}} \iiint_{\text{volume of jet}} \frac{\Gamma[\nu + (1/2)]}{\Gamma(\nu)} \left(\frac{\hat{q}_s^2}{c^2}\right) \frac{\ell_s^3}{\tau_s} \times \frac{|p_a(\mathbf{x_2}, \mathbf{x}, \omega)|^2 e^{-[\omega^2 \ell_s^2/\bar{u}^2 4(\ell_n 2)]}}{\{1 + \omega^2 \tau_s^2 [1 - (\bar{u}/a_\infty)\cos\Theta]^2\}^{\nu + (1/2)}} \mathbf{dx_2} \tag{32}$$

For convenience, we use D_p and D_s to denote the nozzle exit diameters of the primary and secondary jet (see Fig. 4) and u_p and u_s to denote the fully expanded velocities. In Eq. (32), $p_a(\mathbf{x_2}, \mathbf{x}, \omega)$ is the adjoint Green's function and $\omega = 2\pi f$ is the angular frequency. For an installed jet, the computation of the adjoint Green's function is not straightforward. Here, it is computed using a time domain approach. The adjoint Green's function includes the presence of the wing flap and thus accounts for sound reflection by these surfaces (see Appendix). The Gamma function is denoted by $\Gamma(\nu)$, $\bar{u}$ is the mean flow velocity of the jet at the source point $\mathbf{x_2}$, p_{ref} is the reference pressure for the decibel scale, and a_∞ is the ambient sound speed. The quantities (q_s^2/c^2), ν, ℓ_s, and T_s are related to k and ε of the $k - \varepsilon$ turbulence model as follows:

$$\nu = \frac{1}{2} + \begin{cases} c_\eta \frac{k^{3/2}}{\varepsilon} \frac{1}{\rho} \frac{|(\nabla u)\cdot(\nabla \rho)|}{|\nabla u|} \\ 0 \end{cases} \tag{33}$$

$$\frac{\hat{q}_s^2}{c^2} = A^2 q^2 + \begin{cases} B \frac{k^{3/2}}{\varepsilon} \frac{1}{\rho} \frac{|(\nabla u)\cdot(\nabla \rho)|}{|\nabla u|} q^2 \\ 0 \end{cases} \tag{34}$$

$$\ell_s = c_\ell \frac{k^{3/2}}{\varepsilon} + \begin{cases} c_{\ell\rho} \frac{k^3}{\varepsilon^2} \frac{1}{\rho} \frac{|(\nabla u)\cdot(\nabla \rho)|}{|\nabla u|} \\ 0 \end{cases} \tag{35}$$

$$\tau_s = c_\tau \frac{k}{\varepsilon} + \begin{cases} c_{\tau\rho} \frac{k^{5/2}}{\varepsilon^2} \frac{1}{\rho} \frac{|(\nabla u)\cdot(\nabla \rho)|}{|\nabla u|} \\ 0 \end{cases} \tag{36}$$

The formulas on the top of the right-hand side of Eqs. (33–36), are to be used when $(\nabla u) \cdot (\nabla \rho)$ is negative, otherwise the formulas on the bottom right-hand side are to be used. The three constants A, c_ℓ, and c_τ were determined empirically by Tam and Auriault [15] and they were assigned the values

$$A = 0.755, \qquad c_\ell = 0.256, \qquad c_\tau = 0.233$$

The remaining four constants were given the values

$$c_\eta = 2.1599, \qquad B = 0.806$$
$$c_{\ell\rho} = -0.026, \qquad c_{\tau\rho} = -0.2527$$

in [12].

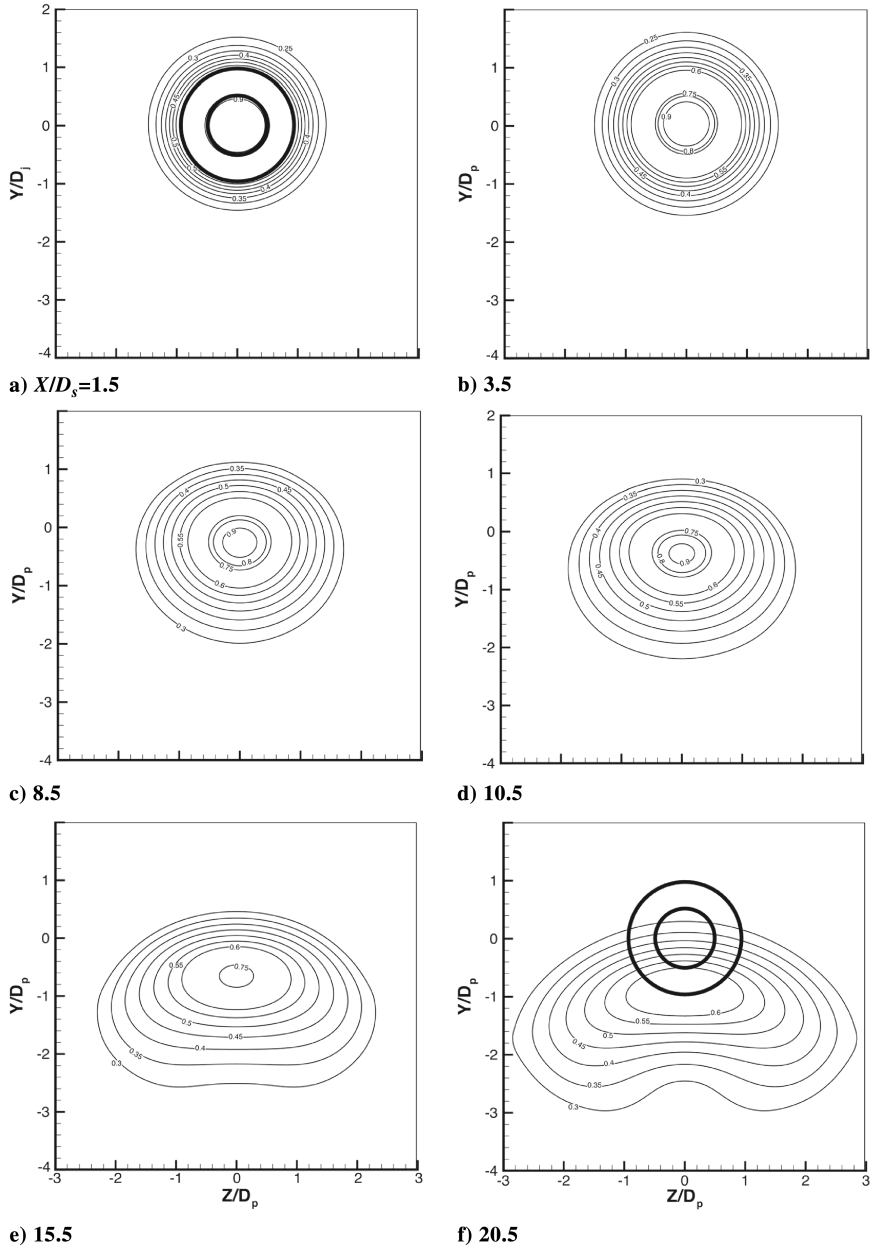

Fig. 5 Contours of axial velocity of a dual stream; flap deflection angle 35 deg, $M_p = 0.762, T_p/T_a = 2.9, M_s = 0.9, T_s/T_a = 1.2, M_f = 0.28$; area ratio 3, bypass ratio 6 dual-stream nozzle.

By means of the formulas in Eqs. (31) and (32), the noise of the installed jet whose mean flow velocity profiles are given in Figs. 5 and 6 are computed. By subtracting out the noise of the same jet in isolation, the installation noise Δ is found. Figure 7 shows a comparison of the computed installation noise spectrum from the fine-scale turbulence of the jet and experimental measurements of Bhat and Blackner [8]. The flap is at a deflection angle of 35 deg. The measurement microphone is at an inlet angle of 90 deg in the flyover plane. As can be seen, the computed installation noise spectrum at high Strouhal number is in good agreement with measurements. However, at intermediate Strouhal number, the measured spectrum has a high level of installation noise that is not predicted by the present model. Figure 8 shows a similar comparison at an inlet angle of 120 deg. There are similar agreement and disagreement with measurements at the 90 deg inlet angle. Figures 9 and 10 show similar comparisons at a flap deflection angle of 23 deg. Again, similar results as at 35 deg deflection angle are found.

Clearly, the present model does not predict a mid-Strouhal number increase in installation noise. However, we believe that the mid-Strouhal number installation noise is from the large turbulence structures of the jet flow. For this reason, the present fine-scale turbulence noise model is unable to correctly predict the entire installation noise spectrum. It is to be noted that large turbulence structures noise of a jet generally peaks at a lower Strouhal number than that of the fine-scale turbulence noise. These large turbulence structures have a near pressure field that extends well outside the jet. This extended field moves downstream with the large turbulence structures. They impinge on the flap when it is deployed at a large angle. The interaction with the flap leads to acoustic scattering and hence noise radiation. We believe this is the mechanism responsible for the observed mid-Strouhal number installation noise. If this explanation is accepted, then the prediction of the present model is in good agreement with experimental measurements. This may also be interpreted as providing a confirmation of the original finding of [9] that the downwash from the wing flap has a dominant effect on installation noise.

V. Conclusions

In this work, the effect of the downwash from a wing-flap combination on an under-the-wing mounted dual-stream jet is investigated. It is found that at large flap deflection angle, the jet flow

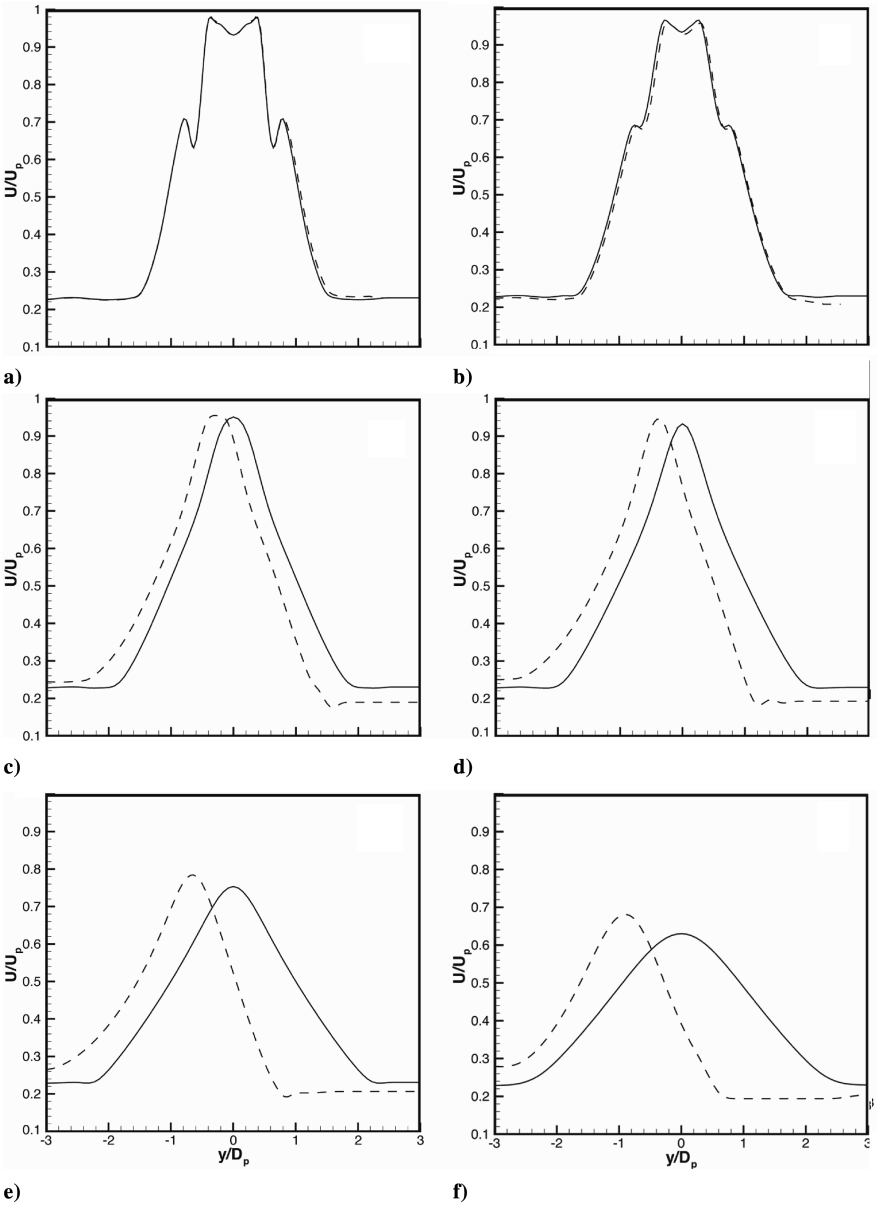

Fig. 6 Comparisons between velocity profiles in the vertical plane through the center of the jet; solid line: isolated jet; dashed line: installed jet. Flap deflection angle 30 deg. Jet operating conditions the same as Fig. 5.

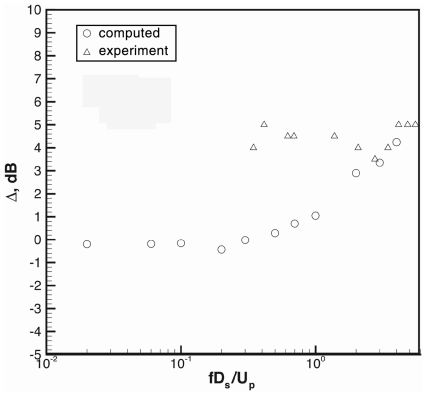

Fig. 7 Installation noise. Flap deflection angle 35 deg. Inlet angle $\chi = 90.0$ deg, $M_p = 0.762$, $T_p/T_a = 2.9$; $M_s = 0.9$, $T_s/T_a = 1.2$, $M_f = 0.28$; area ratio 3, bypass ratio 6 dual-stream nozzle.

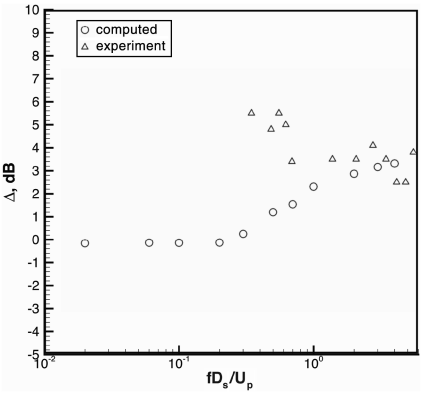

Fig. 8 Installation noise. Flap deflection angle 35 deg. Inlet angle $\chi = 120.0$ deg, $M_p = 0.762$, $T_p/T_a = 2.9$; $M_s = 0.9$, $T_s/T_a = 1.2$, $M_f = 0.28$; area ratio 3, bypass ratio 6 dual-stream nozzle.

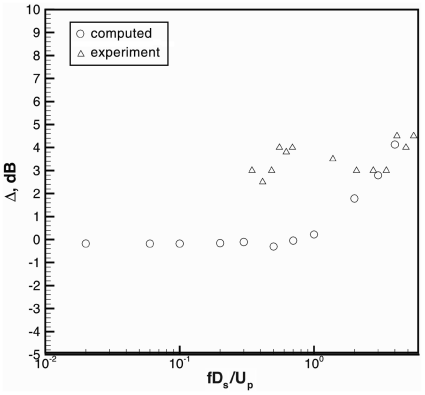

Fig. 9 Installation noise. Flap deflection angle 23 deg. Inlet angle $\chi = 90.0$ deg, $M_p = 0.762$, $T_p/T_a = 2.9$; $M_s = 0.9$, $T_s/T_a = 1.2$, $M_f = 0.28$; area ratio 3, bypass ratio 6 dual-stream nozzle.

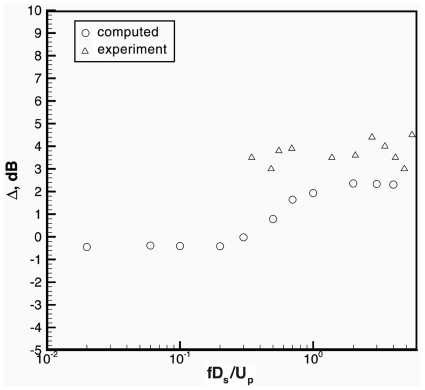

Fig. 10 Installation noise. Flap deflection angle 23 deg. Inlet angle $\chi = 120.0$ deg, $M_p = 0.762$, $T_p/T_a = 2.9$; $M_s = 0.9$, $T_s/T_a = 1.2$, $M_f = 0.28$; area ratio 3, bypass ratio 6 dual-stream nozzle.

is forced downward and distorted laterally. The deflected jet flow is computed using a set of parabolized RANS equations with a modified $k - \varepsilon$ turbulence model. Numerical results reveal that there is an increase in turbulence level in the jet flow. The noise radiated by the fine-scale turbulence of the jet is then calculated by means of the extended Tam and Auriault theory [15,16]. By subtracting out from the computed noise spectrum the noise of the same jet in a standalone condition, the installation noise from the fine-scale turbulence of the jet is determined.

Comparisons between calculated installation noise and experimental measurements are made. It is found that there are good agreements at the high Strouhal number range. However, measurements indicate a significant level of installation noise in the mid-Strouhal number range that is not predicted by the computation. It is, however, the contention of the authors that the discrepancy is not a fault of the computational model, rather that the mid-Strouhal number installation noise is generated by a different mechanism that is beyond the scope of the present investigation. In a jet flow, both large turbulence structures and fine-scale turbulence generate noise. The dominant frequencies of large turbulence structures noise are known to be lower than that of the fine-scale turbulence. In addition, large turbulence structures of a jet have pressure fields extending well outside the jet. The scattering of the extended pressure field by a deployed flap as the large turbulence structures propagate downstream is believed to be the mechanism responsible for generating the mid-Strouhal number installation noise.

In the present model, because the flow interaction between the wing and the jet is highly complex, only the dominant effect, namely, the downwash from the wing on the jet, is taken into account. It is possible to include the effect of the jet on the wing flow by modeling the jet as a line source. A good estimate of the source distribution is to use the entrainment flow of an isolated jet. This improved model will probably become necessary when the engine is mounted much closer to the wing than is presently the practice in industry.

Finally, it is the authors' belief that there is now a computational model by which high-frequency installation noise from fine-scale turbulence of an installed jet may be computed. Because only a limited amount of experimental data are available at the present time, it has not been possible to perform extensive validation of the computation model. Further comparisons are beneficial and necessary. In addition, there is a great need for the development of a large turbulence structures jet noise prediction theory. In the absence of such a theory, a complete prediction of installation jet noise would be very difficult, if not impossible.

Appendix: Adjoint Green's Function

In this appendix, the procedure by which the adjoint Green's function is computed is discussed briefly. To facilitate the computation, the following simplifying assumptions are adopted.

1) The wing flaps are assumed to be long compared with the diameter of the jet so that they may be regarded as effectively infinitely long.

2) The open wind tunnel in the Boeing experiment is very wide. To be consistent with assumption 1, it is taken as infinitely wide or two-dimensional as well.

3) The observer (or measurement microphone) is positioned at or near the flyover plane outside the open wind-tunnel flow.

4) The spreading rate of the jet is small so that the mean flow may be considered locally parallel.

The governing equations for the adjoint Green's function have previously been derived by Tam and Auriault [27]. They have also showed that the boundary condition on a solid surface for the adjoint variables is

$$v_j^{(a)} \cdot n_j = 0 \tag{A1}$$

where n_i is the unit normal of the surface. Superscript (a) denotes an adjoint Green's function variable.

Under the locally parallel flow approximation, the governing equations for the adjoing Green's function are

$$-i\omega\bar{\rho}u^{(a)} - \bar{\rho}\,\bar{u}\frac{\partial u^{(a)}}{\partial x} - \gamma\bar{p}\frac{\partial p^{(a)}}{\partial x} = 0 \tag{A2}$$

$$-i\omega\bar{\rho}v^{(a)} + \bar{\rho}u^{(a)}\frac{\partial \bar{u}}{\partial y} - \bar{\rho}\,\bar{u}\frac{\partial v^{(a)}}{\partial x} - \gamma\bar{p}\frac{\partial p^{(a)}}{\partial y} - (\gamma-1)p^{(a)}\frac{\partial \bar{p}}{\partial y} = 0 \tag{A3}$$

$$-i\omega\bar{\rho}w^{(a)} + \bar{\rho}u^{(a)}\frac{\partial \bar{u}}{\partial z} - \bar{\rho}\,\bar{u}\frac{\partial w^{(a)}}{\partial x} - \gamma\bar{p}\frac{\partial p^{(a)}}{\partial z} - (\gamma-1)p^{(a)}\frac{\partial \bar{p}}{\partial z} = 0 \tag{A4}$$

$$-i\omega p^{(a)} - \left(\frac{\partial u^{(a)}}{\partial x} + \frac{\partial v^{(a)}}{\partial y} + \frac{\partial w^{(a)}}{\partial z}\right) - \bar{u}\frac{\partial p^{(a)}}{\partial x} = \frac{1}{2\pi}\delta(\mathbf{x} - \mathbf{x_0}) \tag{A5}$$

Outside the open wind tunnel, Eqs. (A1–A5) reduce to

$$\mathbf{v}^{(a)} = i\frac{a_\infty^2}{\omega}\nabla p^{(a)} \tag{A6}$$

$$\nabla^2 p^{(a)} + \frac{\omega^2}{a_\infty^2}p^{(a)} = \frac{i\omega}{2\pi a_\infty^2}\delta(\mathbf{x} - \mathbf{x_0}) \tag{A7}$$

The solution of Eq. (A7) is

$$p^{(a)}(\mathbf{x}, \mathbf{x_0}) = -\frac{i\omega}{8\pi^2 a_\infty^2}\frac{e^{i(\omega/a_\infty)|\mathbf{x}-\mathbf{x_0}|}}{|\mathbf{x} - \mathbf{x_0}|} \tag{A8}$$

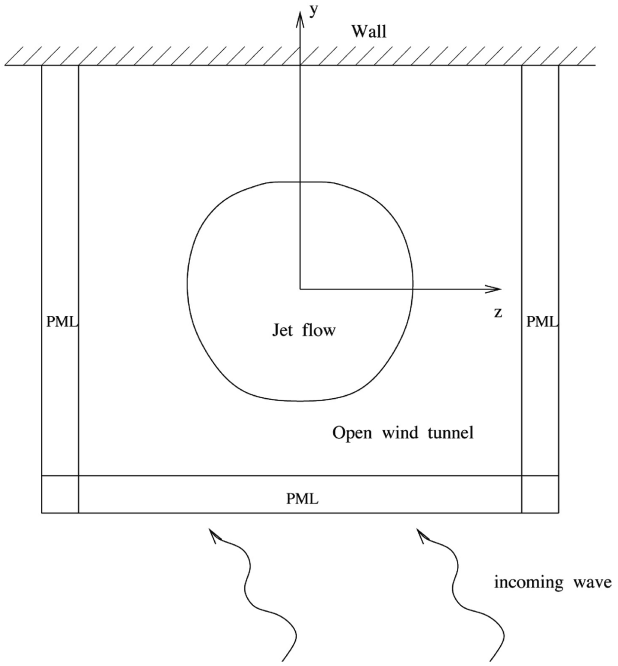

Fig. A1 Computational domain for adjoint Green's function.

It is advantageous to rewrite Eq. (A8) with respect to a spherical polar coordinate system centered at the exit of the primary nozzle with the polar axis coinciding with the direction of jet flow, that is, the same as the x axis. Let the spherical polar coordinates of the observer microphone be (R, Θ, ϕ), then for $R \to \infty$

$$|\mathbf{x} - \mathbf{x_0}| = R - \frac{\mathbf{x} \cdot \mathbf{x_0}}{R} = R - x\cos\Theta - y\sin\Theta\cos\phi - z\sin\Theta\sin\phi \tag{A9}$$

Substitution of Eq. (A9) into Eq. (A8), and upon using Eq. (A6), the adjoint Green's function outside the open wind tunnel becomes

$$\begin{bmatrix} u^{(a)} \\ v^{(a)} \\ w^{(a)} \\ p^{(a)} \end{bmatrix} = -\frac{i\omega}{8\pi^2 a_\infty^2 R} \begin{bmatrix} a_\infty\cos\Theta \\ a_\infty\sin\Theta\cos\phi \\ a_\infty\sin\Theta\sin\phi \\ 1 \end{bmatrix} e^{i(\omega/a_\infty)[R - x\cos\Theta - y\sin\Theta\cos\phi - z\sin\Theta\sin\phi]} \tag{A10}$$

Equation (A10) represents an incoming wave toward the open wind tunnel and the jet as shown in Fig. A1. By invoking the locally parallel flow approximation, it becomes clear that the full solution must have the same x dependence as Eq. (A10). Thus, the factor $\exp[-i(\omega/a_\infty)x\cos\Theta]$ can be factored out from the problem. This reduces the problem effectively to two-dimensional in y and z.

The jet and the open wind tunnel will cause scattering to the incoming wave. To compute the adjoint Green's function inside the open wind tunnel and the jet, a simple way is first to omit the jet flow and calculate the reflected and transmitted wave for the wind-tunnel flow alone. For the portion of the jet located directly under the wing flap, the wing flap is modeled by a solid surface as shown in Fig. A1. For the portion of the jet located downstream of the wing flap, there is no solid wall. The reflection boundary condition at the wing is replaced by a transmitted wave. This problem can be greatly simplified by separating out the z dependence in the form given by Eq. (A10). The problem then reduces to two ordinary differential equations that can readily be integrated.

The second step is to insert the jet flow back in the open wind tunnel. The mathematical problem as posed becomes a purely two-dimensional scattering problem. The scattering problem can best be solved by separating out the x dependence in Eqs. (A1–A5) as mentioned before. The simplified two-dimensional problem can then be solved by using a time marching scheme. The computational domain is as shown in Fig. A1. We find it most convenient to use a perfectly matched layer [28] (PML) as absorbing boundary condition for the scattered waves. In this work, the seven-point stencil diepersion-relation-preserving scheme is used. The computation is stable and efficient. The time marching computation continues until a time periodic solution is obtained.

Acknowledgment

This work was supported by NASA Langley Research Center Contract NAS1-01045.

References

[1] Way, D. J., and Turner, B. A., "Model Tests Demonstrating Under-Wing Installation Effects on Engine Exhaust Noise," AIAA Paper 80-1048, 1980.

[2] Wang, M. E., "Wing Effect on Jet Noise Propagation," AIAA Paper 80-1047, 1980.

[3] Reddy, N. N., and Tanna, H. K., "Installation Effects on Jet Noise in Flight," AIAA Paper 80-1044, 1980.

[4] Stevens, R. C. K., Bryce, W. D., and Szewczyk, V. M., "Model and Full-Scale Studies of the Exhaust Noise from a Bypass Engine in Flight," AIAA Paper 83-0751, 1983.

[5] Mead, C. J., and Strange, P. J. R., "Under-Wing Installation Effects on Jet Noise at Sideline," AIAA Paper 98-2208, 1998.

[6] Shivashankara, B. N., and Blackner, A. M., "Installed Jet Noise," AIAA Paper 97-1601, 1997.

[7] Blackner, A. M., and Bhat, T. R. S., "Installation Effects on Coaxial Jet Noise: An Experimental Study," AIAA Paper 98-0080, 1998.

[8] Bhat, T. R. S., and Blackner, A. M., "Installed Jet Noise Prediction Model for Coaxial Jets," AIAA Paper 98-0079, 1998.

[9] Bhat, T. R. S., "Jet-Flap Installation Noise," NASA Contractor Final Report on Contract NAS 1-20267, Task 17, Subtask 2, Jan. 1998.

[10] Lu, H. Y., "An Empirical Model for Prediction of Coaxial Jet Noise in Ambient Flow," AIAA Paper 86-1912, 1986.

[11] Mengle, V. G., Elkoby, R., Brusniak, L., and Thomas, R. H., "Reducing Propulsion Airframe Aeroacoustic Interactions with Uniquely Tailored Chevrons, 1: Isolated Nozzles," AIAA Paper 2006-2467, May 2006.

[12] Mengle, V. G., Elkoby, R., Brusniak, L., and Thomas, R. H., "Reducing Propulsion Airframe Aeroacoustic Interactions with Uniquely Tailored Chevrons, 2: Installed Nozzles," AIAA Paper 2006-2434, May 2006.

[13] Mengle, V. G., Elkoby, R., Brusniak, L., and Thomas, R. H., "Reducing Propulsion Airframe Aeroacoustic Interactions with Uniquely Tailored Chevrons, 3: Jet-Flap Interaction," AIAA Paper 2006-2435, May 2006.

[14] Nesbitt, E., Mengle, V. G., Callender, B., and Thomas, R. H., "Flight Test Results for Uniquely Tailored Propulsion Airframe Aeroacoustic Chevrons: Community Noise," AIAA Paper 2006-2438, May 2006.

[15] Tam, C. K. W., and Auriault, L., "Jet Mixing Noise from Fine Scale Turbulence," *AIAA Journal*, Vol. 37, No. 2, 1999, pp. 145–153.

[16] Tam, C. K. W., Pastouchenko, N. N., and Viswanathan, K., "Fine Scale Turbulence Noise from Hot Jets," AIAA Paper 2004-0362, Jan. 2004.

[17] Tam, C. K. W., and Kurbatskii, K. A., "Multi-Size-Mesh Multi-Time-Step Dispersion-Relation-Preserving Scheme for Multiple-Scales Aeroacoustics Problems," *International Journal of Computational Fluid Dynamics*, Vol. 17, No. 2, 2003, pp. 119–132. doi:10.1080/1061856031000104860

[18] Kurbatskii, K. A., and Tam, C. K. W., "Cartesian Boundary Treatment of Curved Walls for High-Order Computational Aeroacoustics Schemes," *AIAA Journal*, Vol. 35, No. 1, 1997, pp. 133–140.

[19] Tam, C. K. W., and Webb, J. C., "Dispersion-Relation-Preserving Finite Difference Scheme for Computational Acoustics," *Journal of Computational Physics*, Vol. 107, Aug. 1993, pp. 262–281. doi:10.1006/jcph.1993.1142

[20] Tam, C. K. W., and Dong, Z., "Radiation and Outflow Boundary Conditions for Direct Computation of Acoustic and Flow Disturbances in a Nonuniform Mean Flow," *Journal of Computational Acoustics*, Vol. 4, No. 2, 1996, pp. 175–201. doi:10.1142/S0218396X96000040

[21] Pope, S. B., "An Explanation of the Turbulent Round Jet/Plane Jet Anomaly," *AIAA Journal*, Vol. 16, No. 3, 1978, pp. 279–281.

[22] Sarkar, S., and Lakshmanan, B., "Application of a Reynolds Stress Turbulence Model to the Compressible Shear Layer," *AIAA Journal*, Vol. 29, No. 5, 1991, pp. 743–749.

[23] Tam, C. K. W., and Ganesan, A., "A Modified k-ε Turbulence Model for Calculating Hot Jet Mean Flow and Noise," *AIAA Journal*, Vol. 42, No. 1, 2004, pp. 26–34.

[24] Thies, A. T., and Tam, C. K. W., "Computation of Turbulent Axisymmetric and Nonaxisymmetric Jet Flows Using the k-ε Model," *AIAA Journal*, Vol. 34, No. 2, 1996, pp. 309–316.

[25] Tam, C. K. W., Pastouchenko, N. N., and Auriault, L., "Effects of Forward Flight on Jet Mixing Noise from Fine Scale Turbulence," *AIAA Journal*, Vol. 39, No. 7, 2001, pp. 1261–1269.

[26] Tam, C. K. W., and Pastouchenko, N. N., "Fine Scale Turbulence Noise from Dual Stream Jets," *AIAA Journal*, Vol. 44, No. 1, 2006, pp. 90–101.

[27] Tam, C. K. W., and Auriault, L., " Mean Flow Refraction Effects on Sound Radiated from Localized Sources in a Jet," *Journal of Fluid Mechanics*, Vol. 370, 1998, pp. 149–174. doi:10.1017/S0022112098001852

[28] Hu, F. Q., "A Stable, Perfectly Matched Layer for Linearized Euler Equations in Unsplit Physical Variables," *Journal of Computational Physics*, Vol. 173, 2001, pp. 455–480. doi:10.1006/jcph.2001.6887

R. So
Associate Editor